PAPER

Origami-inspired self-deployment 4D printed honeycomb sandwich structure with large shape transformation

View the article online for updates and enhancements.

Origami-inspired self-deployment 4D printed honeycomb sandwich structure with large shape transformation

Xiaozhou Xin[1] , **Liwu Liu**[1], **Yanju Liu**[1] **and Jinsong Leng**[2]

[1] Department of Astronautical Science and Mechanics, Harbin Institute of Technology (HIT),
P.O. Box 301, No. 92 West Dazhi Street, Harbin 150001, People's Republic of China
[2] National Key Laboratory of Science and Technology on Advanced Composites in Special Environments,
Harbin Institute of Technology (HIT), No.2 Yikuang Street, P.O. Box 3011, Harbin 150080,
People's Republic of China

E-mail: liuliwu_006@163.com and lengjs@hit.edu.cn

Abstract

4D printing provides more design freedom for the static structures by adding time dimension in 3D printing. In recent years, some types of active origami structures fabricated by 4D printing have been developed, but most of these structures were thin sheets, which may lead to poor mechanical properties of the structures. In this work, honeycomb sandwich structures were designed to improve the stiffness and recovery force of origami structures. The in-plane tension, in-/out-plane three-point bending, recovery force and shape memory performances of the sandwich structures were investigated. The shape fixity and shape recovery ratio of the active sandwich structures were 98% and 99%, indicating excellent shape memory performance. The application of the sandwich structures in thermally activated self-deployment origami structures was verified. These developed origami structures have the advantages of large area change ratio and fast response speed, demonstrating the great application prospects in the space deployable structures such as antennas.

Keywords: 4D printing, shape memory polymers, origami structure, self-deployment

(Some figures may appear in colour only in the online journal)

1. Introduction

Shape memory polymers (SMPs) are stimulus-responsive materials with the ability to maintain a desirable temporary shape and recover to its original shape under specific stimuli (heat, electricity, magnetism, etc) [1–6]. It has inspired a wide range of academic and engineering interests over the past few decades. SMPs-based structures with self-deployment capability have broad application prospects in bioengineering, microelectromechanical systems (MEMS) and robotics, especially in space deployable structures [7–16]. However, the transport cost and packing size of deployable structures pose challenges to the shrinkage ratio of structures.

Origami, emerging in China and Japan in the 1600 s or earlier, can create three-dimensional (3D) configuration from two-dimensional (2D) paper by accurately folding predefined creases [17]. Conversely, the structure can also morph from 3D configuration into a flat. This unique shape-transition characteristic and large area change ratios provide solutions to package and transport large objects. The origami-inspired mirror/solar panels, human lunar bases and bifurcated stents have been developed [18–26]. Nevertheless, the complexity of configuration transformation of origami structures usually requires automation infrastructures to achieve orderly and controllable deformation. Fortunately, the active origami structures made of stimulus-responsive materials with self-deployment properties can effectively reduce the use of these devices [27, 28]. In addition, 4D printing refers to the combination of 3D printing and intelligent materials, which endows static structure with features of self-assembly, self-adaptive, multi-functional and reconfiguration, and provides more design freedom for active origami structure [29–32].
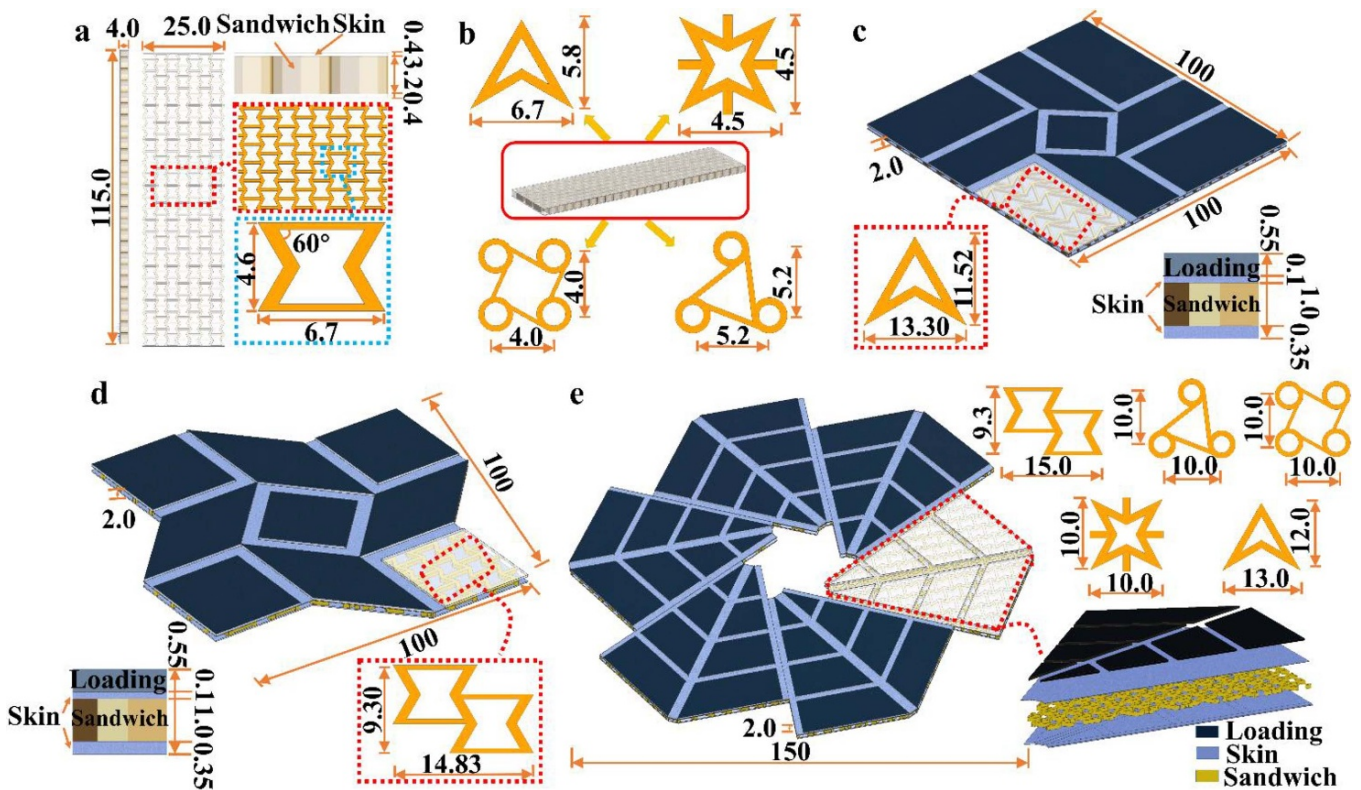
Figure 1. 3D CAD models of active sandwich structures, cells and self-deployment origami structures: (a) ST-Re, (b) ST-Do, ST-St, ST-6c and ST-4c, (c) OS-Tw, (d) OS-Sq, and (e) OS-AS.

Although there have been some studies on 4D printing origami structures [33–39], these works mainly focus on the intelligent deformation and geometric characteristics of origami structures. Most existing origami structures are thin sheet structures, which results in poor mechanical properties of the structures. This problem can be solved by increasing the thickness of the sheet, but the area change ratio of the structure will be decreased.

The purpose of this work was to design origami structures with foldability, self-deployment origami structures with excellent mechanical properties. The self-deployment performance of origami structure was realized through the understanding of shape memory process. The structure can be folded at high temperature, and the temporary shape was fixed at low temperature. When reheated, the structure deployed itself to its original shape. The temperature-dependent self-deployment active sandwich structures were developed to improve the stiffness, strength and recovery force of origami. Some types of honeycombs, including re-entrant, hexa-chiral, tetra-chiral, star-shaped, and double arrowhead, were selected as the sandwich layer due to their unique energy absorption ability and lightweight characteristic [39–42]. The in-plane tension, in-/out-plane three-point bending, recovery force and shape memory properties of active sandwich structures were systematically investigated. Finally, combining the active sandwich structures and origami art, three types of origami-inspired self-deployment structures were demonstrated.

2. Design, materials, and methods

2.1. Design of active sandwich and origami structures

3D CAD model of active sandwich structure with re-entrant honeycomb is shown in figure 1(a). The upper and lower surfaces of the structure were covered with skin with a thickness of 0.4 mm. The designed skin can improve the smoothness in the process of thermomechanical programming. The honeycomb unit cells with the dimension of 6.7 mm × 4.6 mm × 3.2 mm periodically distributed along with the longitudinal and transverse directions of the sandwich structures. In addition, four other active sandwich lays were designed, including hexa-chiral, tetra-chiral, star-shaped, and double arrowhead honeycomb (figure 1(b)). For the convenience of presentation, ST-Re, ST-6c, ST-4c, ST-St, and ST-Do were used to represent the sandwich structure with re-entrant, hexa-chiral, tetra-chiral, star-shaped, and double arrowhead honeycomb, respectively.

The active sandwich structures were popularized in the origami-inspired self-deployment structures. Figure 1(c) demonstrates the twistable origami structure (denoted by OS-Tw) derived from ST-Do. Figure 1(d) exhibits the square-twist structure (denoted by OS-Sq) extended by ST-Re. Figure 1(e) displays the array structure (denoted by OS-AS). In this work, OS-AS-Re, OS-AS-6c, OS-AS-4c, OS-AS-St, and OS-AS-Do were used to denote OS-AS derived from ST-Re, ST-6c, ST-4c, ST-St, and ST-Do respectively. The dimensions of OS-Tw, OS-Sq, and OS-AS at the original shape were
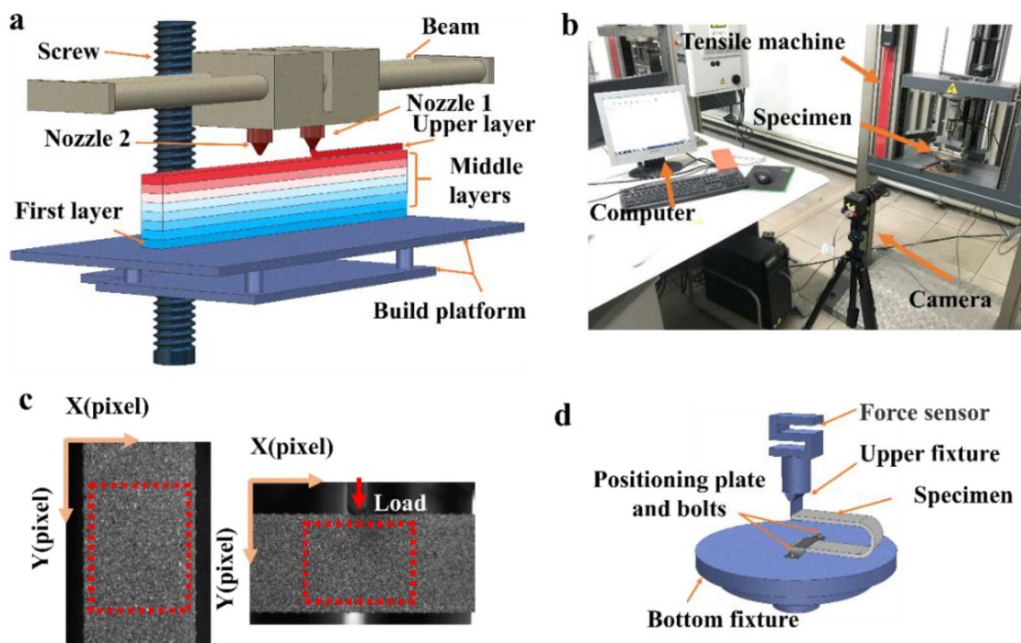
Figure 2. (a) FDM printing process. The first layer of PLA on the build platform has a lower temperature and the upper layer has a higher temperature. Characterization of mechanical properties: (b) loading diagram of tensile and three-point bending test; (c) speckles and analysis areas (rectangle with red dotted lines) of in-plane tension (left) and in-plane three-point bending (right); (d) schematic diagram of active sandwich structure recovery force test.

100 mm × 100 mm × 2.0 mm, 100 mm × 100 mm × 2.0 mm, and 150 mm × 150 mm × 2.0 mm, respectively. The folding states of three types of self-deployment origami structures were referred to [39, 43, 44]. Creases (light blue in figure 1) were designed in origami structure for programming. It was noteworthy that relatively thin creases can effectively reduce damage and fracture during programming. Loading parts (dark blue) were added to the undeformed areas of the structure's upper surface. The thickness of upper and lower skins of three types of origami structures were 0.1 mm and 0.35 mm. The thickness of the loading part was 0.55 mm. The cell size of honeycomb in origami can be obtained in figures 1(c)–(e). For OS-Tw and OS-Sq, the cell was arranged periodically along with the longitudinal and transverse directions of the structure. For OS-AS, the cell distributed periodically in the structural cell (the area surrounded by red dotted lines in figure 1(e)), consisting of two right triangles with overlapping oblique edges. The cell of the structure was distributed in a circular array.

2.2. Materials and methods

Semi-crystalline polylactic acid (PLA)-based shape memory printed filaments with a diameter of 1.75 mm prepared by the research group of Professor Jinsong Leng of Harbin Institute of Technology were employed [38, 45]. Siemens PLM Software UG NX10.0 was used to build 3D CAD models and then saved as STL files. Allcct software was utilized to produce Gcode files and set printing parameters. The samples were fabricated by Allcct 3D printer with two nozzles (ALLCCT Technology Co., Ltd. Wuhan, China). The filling density and the

printing speed were set as 50% and 50 mm min^{-1}, respectively. In addition, the temperatures of the nozzle and build platform were 210 °C and 65 °C, respectively.

Figure 2(a) demonstrates the fused decomposition modeling (FDM) printing process with two heated nozzles. If the nozzle 1 is set to print during deposition, the filament is extruded by the stepping motor from a circular nozzle with a diameter of 0.4 mm. The extruded polymer is deposited onto the platform at the set printing speed and then solidified. Once this layer is completed, the platform moves down to print the next layer in the same way. If the nozzle 2 is switched during the printing process, the nozzle moves a certain distance to the right, which is the relative distance between the two nozzles. This movement is driven by the stepping motor on the beam. The blue PLA-based SMPs filament was utilized to print the loading parts of the origami structure. Since the printed materials were all PLA-based SMPs filaments, it was not necessary to consider the interface debonding problem.

Characterization of dynamic mechanical properties: Dynamic mechanical analysis (DMA) was performed on the DMA Q800 to characterize the thermodynamic behavior of PLA-based SMPs. The printed rectangular sample (20 mm × 5 mm × 2 mm) was first heated to 95 °C and stabilized for 30 min to achieve thermal equilibrium, and then a preload of 0.001 N was applied. During the experiment, the strain oscillated at a frequency of 1 Hz while the temperature was cooled from 95 °C to 25 °C with a speed of 2 °C min^{-1}. The sample was held at 25 °C for 30 min and reheated to 95 °C at the same rate. The above steps were repeated multiple times to release the internal stress and temperature-induced residual strain of the specimen. The data of the last heating step was exported.

Morphology characterization: The morphologies of the printed active sandwich structures were characterized by VEGA3 TESCAN SEM at an accelerating voltage of 20.0 kV.

Mechanical property characterization: The in-plane tension, in-/out-plane three-point bending tests of ST-Do, ST-Re, ST-St, ST-4c, and ST-6c were investigated on the ZWICK-010 stretcher with a loading rate of 2 mm min^{-1}. The samples of in-plane tension test and in-plane three-point bending test are shown in the left and right diagrams of figure 2(c). Before the in-plane tension and in-plane three-point bending tests, the speckle was sprayed on the surface of the active sandwich structures. The strain of the sample's surface was monitored by digital image correlation technology (DIC) during the loading process, as shown in figure 2(b). The optical axis of the CCD camera was approximately perpendicular to the surface of the tested sample to obtain high-quality photographs. The strain in the middle part of the sample was selected for analysis (in the red rectangular in figure 2(c)). Undeformed image was taken as reference. The sample was photographed at intervals of 50 N during the loading process, and the sensor recorded the load and displacement.

Recovery performance characterization: The recovery force tests of ST-Do, ST-Re, ST-St, ST-4c, and ST-6c were performed on a ZWICK-010 stretcher with an environmental chamber. The specimen was placed in the chamber (90 °C) for 15 min before the test. The mold was utilized to program the sample into U-shaped, which will be fixed after cooling to room temperature. The sample with temporary configuration was fixed on the lower fixture through the positioning plate and bolts to prevent the relative displacement between the sample and fixture during the shape memory recovery process. The fixture spacing was adjusted to ensure that the sensor touched the edge of the sample, as shown in figure 2(d). During the test, the temperature of the chamber (90 °C) and the fixture spacing remained unchanged. The force sensor was used to record the change of force.

The shape recovery properties of ST-Do, ST-Re, ST-St, ST-4c and ST-6c were characterized using an environmental chamber with the temperature of 90 °C. Considering the large and complex deformation of the origami structures, the shape memory recovery process was characterized in hot water (90 °C). Video camera (Canon DS126571) was utilized to record this process.

3. Results and discussion

3.1. Dynamic mechanical analysis

The temperature-dependent results in terms of storage modulus (E_S) and tan δ are shown in figure 3. It can be found that E_S of PLA-based SMP was 1826.20 MPa at low temperature (T_l), while it decreased to 5.52 MPa when the temperature was heated to 95 °C (T_h). The phase transition of PLA-based SMPs from glassy phase to the rubbery phase led to a high ratio of E_S downfall equal to ~600. The tan δ peak of PLA-based SMP associated with the glass transition temperature was read as $T_g = 70.35$ °C. In addition, Young's modulus of SMPs can be obtained from DMA test curves by the formula defined as

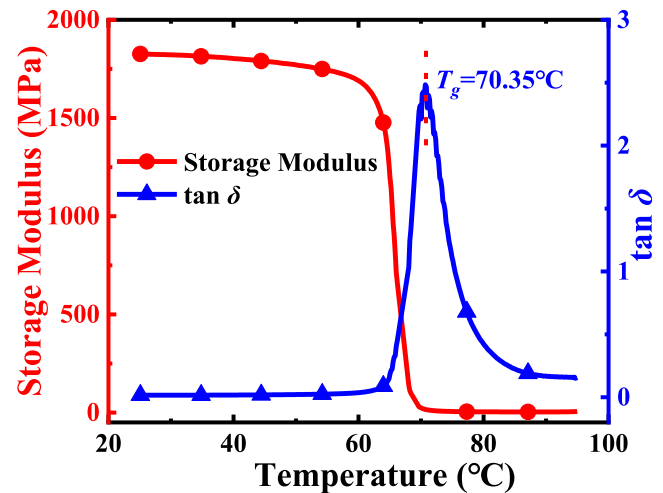**Figure 3.** DMA test curves of PLA-based SMPs.

$E = E_s\sqrt{1 + (\tan\delta)^2}$, $E_g = 1826.45$ MPa and $E_r = 5.57$ MPa for glassy phase and rubbery phase, respectively.

3.2. Morphological characterization

Figure 4(a) exhibits the printed active sandwich structures and SEM images of the honeycomb structures with different cells. The folding state, original shape and CAD model of OS-Sq, OS-Tw and OS-AS are shown in figures 4(b)–(d). The designed crease and loading parts of the origami structure were also printed with high precision. Comparing the folding state with the original shape, it can be found that the volume of the origami structure changed greatly. There was no stratification or fracture between the loading part and sandwich structures of origami structure in the programming process. This proved that the design of creases and thickness of the origami structure was reasonable.

3.3. In-plane tensile properties

The in-plane uniaxial tensile curves and the strain distribution along the Y direction of the sample (ε_y) under partial loads of ST-Re, ST-6c, ST-4c, ST-Do and ST-St are shown in figures 5(a)–(f). The maximum load (L_{max}), tensile strength (σ_f) and elongation (δ) of the active sandwich structures measured by in-plane uniaxial tension test are shown in table 1. The uniaxial tensile strength was calculated according to equation (1).

$$\sigma_f = \frac{F}{bh} \qquad (1)$$

where b is the width of the sample (25 mm) and h is the height (4 mm).

The samples fractured in a brittle manner at room temperature and there was no yield phenomenon during the tensile process. ST-St had the highest load-carrying capacity, while ST-4c had the lowest. The L_{max}/σ_f of ST-St and ST-4c
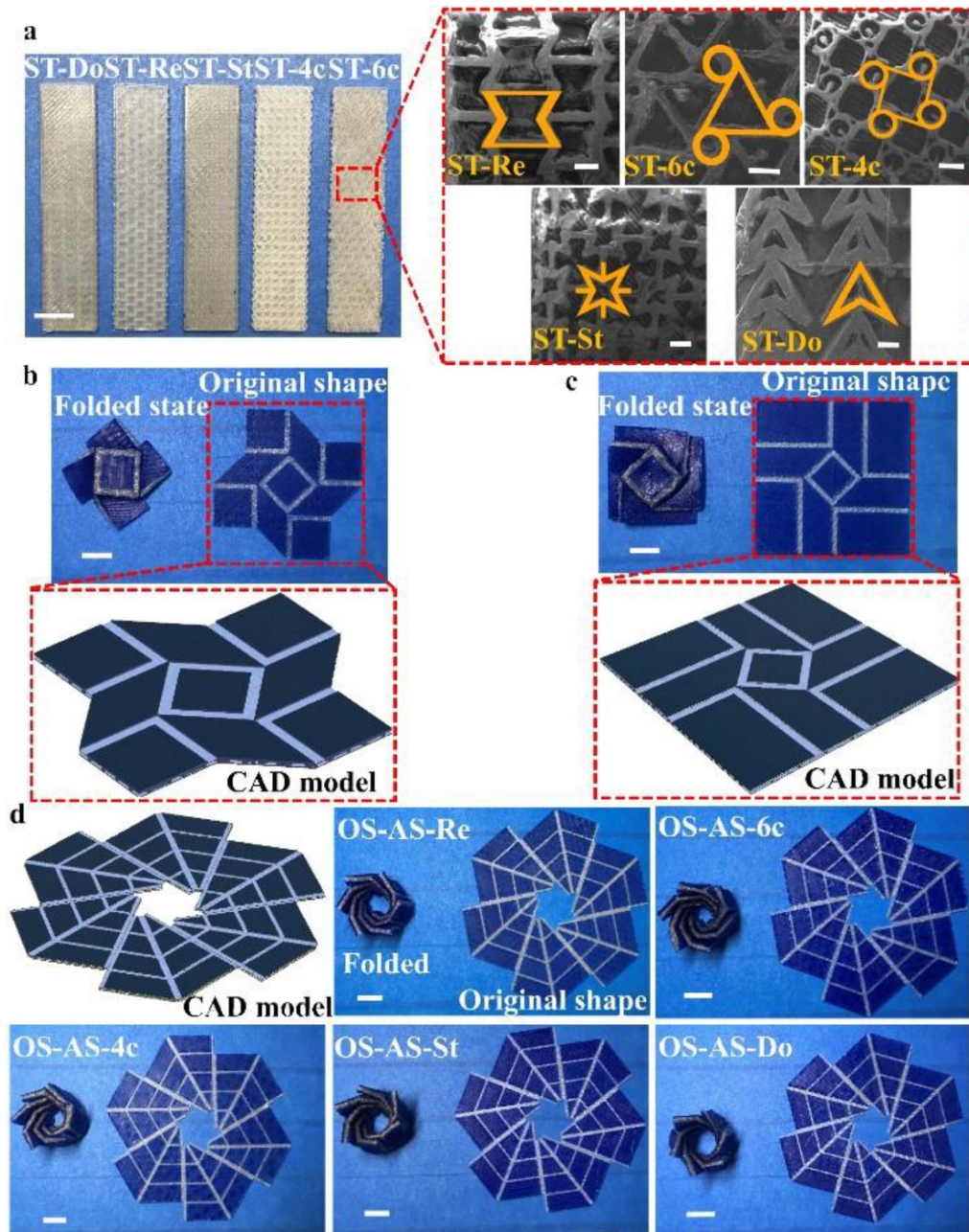
Figure 4. (a) Printed samples with different active sandwich structures, SEM images and CAD models of honeycombs. Folded states, original states and CAD models of (b) OS-Sq, (c) OS-Tw and (d) OS-AS. The scale bar of the SEM image is 2 mm, others is 20 mm.

were 1028.20 N/10.28 MPa and 529.55 N/5.30 MPa, respectively. The δ of ST-St (3.08%) was the lowest, while ST-4c (5.20%) was the highest. There were some differences in the bearing capacity of different active sandwich structures, which may be caused by the difference in the effective cross-sectional area of the sample. When the sample subjected to in-plane tensile load, the maximum stress appeared in the minimum section. The stress of this section reached the fracture strength of the material and microcracks appeared as the load increased.

The ε_y on the sample surface under different loads are plotted in figure 5(a)–(e). The load value and number of the contour plot are marked on the left side of each plot. The strain

values of each pixel under different loads can be obtained by the colour bar and the number of the contour plot. The strain of the specimen increases with the increase of load in the DIC test. For example, when ST-Re subjected to 100 N, the maximum and minimum values of ε_y were 0.235% and -0.007%, respectively. When the load increases to 700 N, the maximum and minimum values of ε_y also increased to 1.40% and 0.746%, respectively. It can be observed that the strain distribution was inhomogeneous on the sample surface. Taking the strain field of ST-6c recorded by DIC when the applied load value was 600 N as an example (shown in figure 5(f)). $\varepsilon_y = 1.59\%$ and 1.09% at point X = 425 pixel, Y = 217 pixel and point X = 425 pixel, Y = 429 pixel, respectively, which
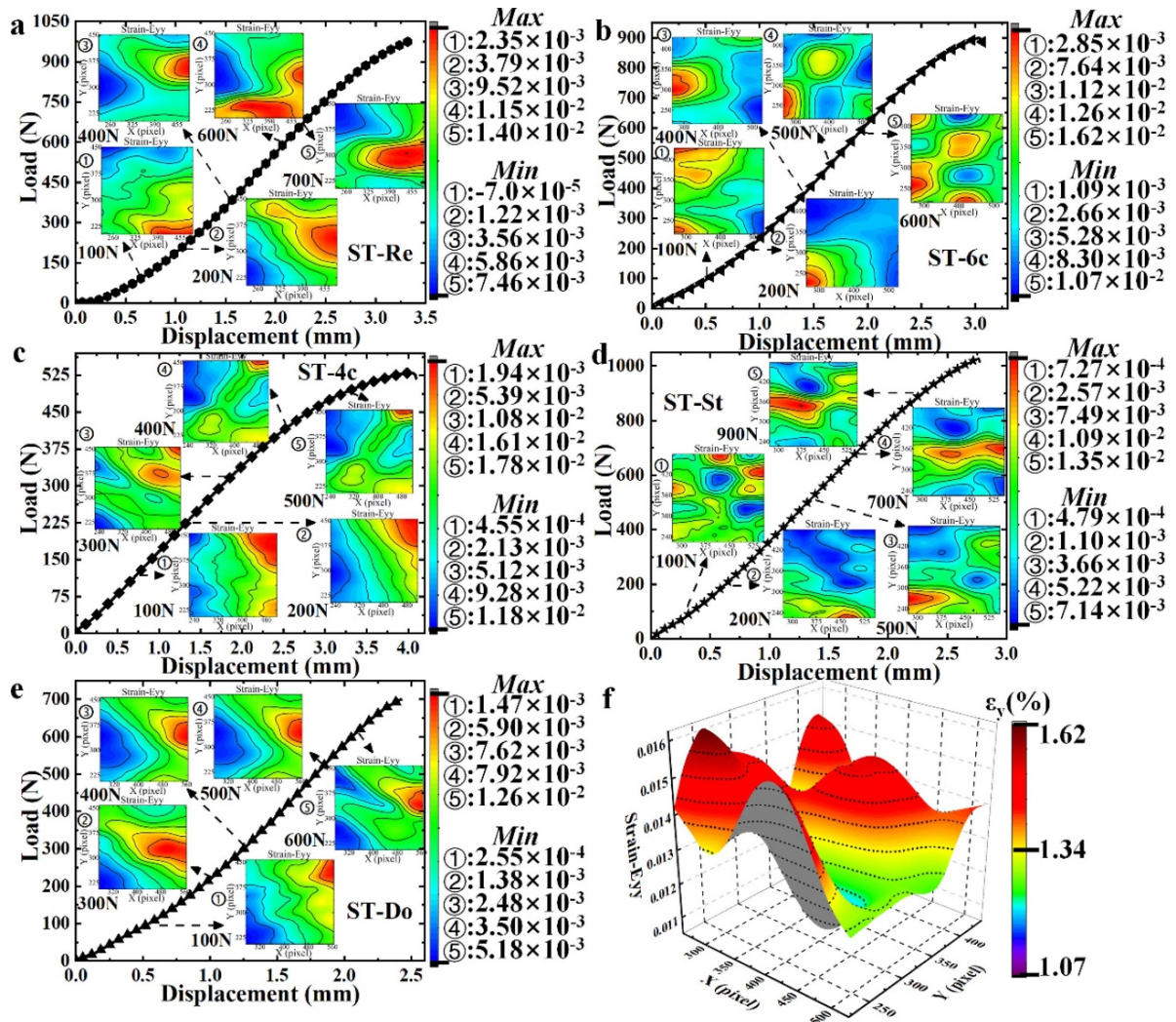
Figure 5. Load-displacement curves and strain fields information of the sample: (a) ST-Re, (b) ST-6c, (c) ST-4c, (d) ST-St, (e) ST-Do and (f) ε_y distribution of ST-6c under 600 N. In (a)–(e), the strain fields under different loads referred to the maximum and minimum strains of each contour plot number in the colour bar.

differed by ~0.5%. This phenomenon of strain inhomogeneity was caused by the mutual restriction of deformation between honeycomb and skin.

3.4. In-plane three-point bending properties

The in-plane three-point bending curves and the strain distribution along the X direction of the sample surface (ε_x) under partial loads of active sandwich structures are plotted in figures 6(a)–(e). The maximum load ($L_{\max}^{in-plane}$), bending strength ($\sigma_f^{in-plane}$) and effective bending modulus ($E_{eff}^{in-plane}$) of the samples are shown in table 1. $\sigma_f^{in-plane}$ and $E_{eff}^{in-plane}$ were calculated according to equation (2) and (3), respectively.

$$\sigma_f = \frac{3Fl}{2bh^2} \qquad (2)$$

$$E_{eff} = \frac{l^3}{48I}\left(\frac{\Delta F}{\Delta \delta}\right) \quad I = \frac{bh^3}{12} \qquad (3)$$

where l is the span length, F is the maximum load value, ΔF is the applied load and $\Delta \delta$ is the deflection of the central point in span.

Similar to the tensile tests, ST-St had the highest strength ($\sigma_f^{in-plane} = 22.86$ MPa, $L_{\max}^{in-plane} = 482.43$ N). Under this load condition, the strength of ST-6c was the lowest ($\sigma_f^{in-plane} = 10.43$ MPa, $L_{\max}^{in-plane} = 220.14$ N). The in-plane bending modulus of ST-St was the highest ($E_{eff}^{in-plane} = 519.37$ MPa), and ST-4c was the lowest ($E_{eff}^{in-plane} = 240.04$ MPa).

The ε_x on the surface of the sample was uniform according to the strain distribution recorded by DIC. The strain fields under different load values referred to the maximum and minimum strains of contour plot number in the colour bar in figures 6(a)–(e). The upper part of the neutral axis of the sample was compressive deformation, while the opposite was tensile deformation. The absolute value ε_x was symmetrically distributed according to the neutral axis. Taking ε_x of ST-4c recorded by DIC when the applied load value was 260 N as an example (shown in figure 6(f)). $\varepsilon_x = -1.57\%$,
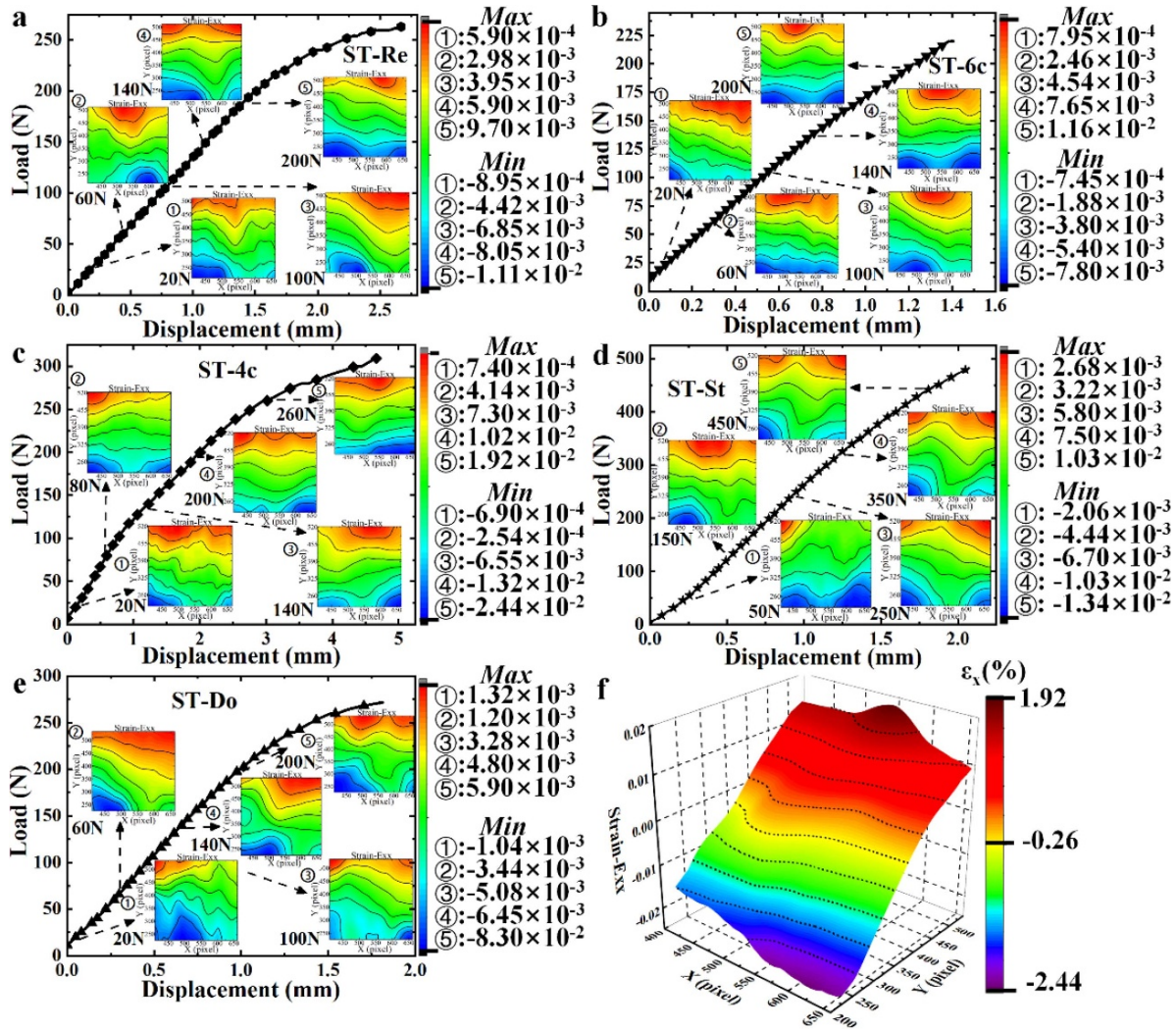
Figure 6. In-plane three-point bending test curves and distribution of ε_x: (a) ST-Re, (b) ST-6c, (c) ST-4c, (d) ST-St, (e) ST-Do, and (f) strain distribution of ST-4c under 260N. In (a)–(e), the strain fields under different loads referred to the maximum and minimum strains of each contour plot number in the colour bar.

−0.07%, and 1.45% at point X = 412 pixel, Y = 219 pixel, point X = 412 pixel, Y = 371 pixel, and point X = 412 pixel, Y = 523 pixel, respectively. It was worth noting that the sample appeared local collapse at the loaded end. The loaded end was the stress concentration area and the sample was a porous material, which resulted in local buckling and out-plane deformation.
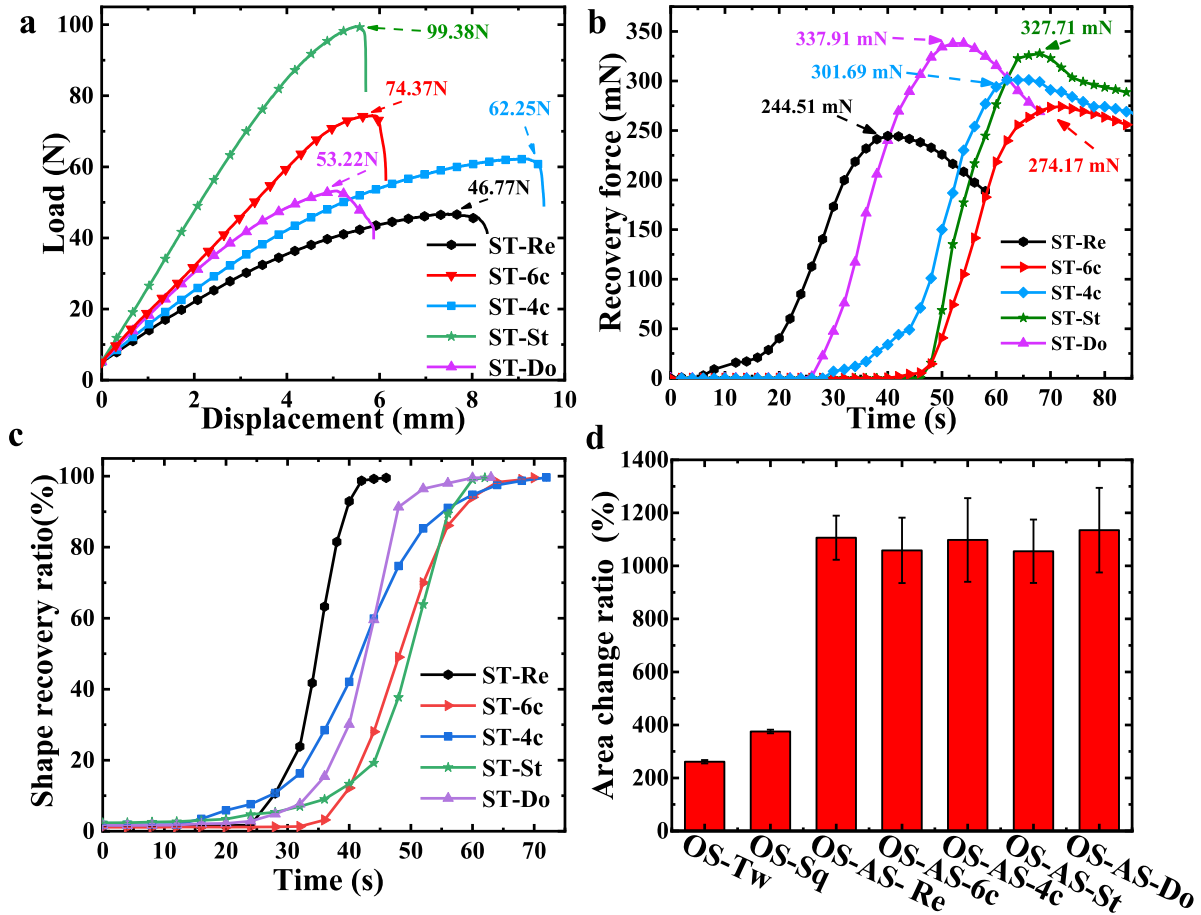
3.5. Out-plane three-point bending properties

The out-plane three-point bending test results of active sandwich structure are shown in figure 7(a). The strength ($\sigma_f^{out-plane}$) and effective bending modulus ($E_{eff}^{out-plane}$) were calculated by equation (2) and (3) under out-plane three-point bending load. During the test, the sample was elastically deformed until failure. ST-St had the best out-plane bending performance ($L_{max}^{out-plane} = 99.38$ N, $\sigma_f^{out-plane} = 29.44$ MPa, and $E_{eff}^{out-plane} = 1817.75$ MPa) and ST-Re was poor ($L_{max}^{out-plane} = 46.77$ N, $\sigma_f^{out-plane} = 13.86$ MPa, and

$E_{eff}^{out-plane} = 826.34$ MPa), which can be obtained through table 1 and figure 7(a).

3.6. Shape recovery properties of active sandwich structures

Figure 7(b) shows the functional relationship between the recovery force and time of the active sandwich structures. The initial recovery force of the test was 0 N since the initial temperature of the sample was room temperature. When the temperature gradually increased to the glass transition region of the sample, the storage strain was activated, leading to a significant change in the recovery force. The storage strain of ST-Re was activated fastest (~10 s), which may be caused by the difference in heat conduction ratio due to the variety of porosity of different sandwich structures. When the temperature of the sample reached near T_g, the recovery force reached the maximum [46]. SMPs transformed from the glassy phase to the rubbery phase completely, which led to a decrease in the stiffness and recovery force of the sandwich structures. ST-Do had

Figure 7. (a) Out-plane three-point bending test curves. (b) Recovery force test curves. (c) Relationship between shape recovery ratio and heating time. (d) The area change ratio of different origami structures.

Table 1. Mechanical and shape memory properties of sandwich structures.

Properties	ST-Re	ST-6c	ST-4c	ST-St	ST-Do
$L_{\max}$(N)	979.11	899.25	529.55	1028.20	699.11
σ_f (MPa)	9.79	8.99	5.30	10.28	6.99
δ (%)	4.25	3.90	5.20	3.08	3.52
$L_{\max}^{in-plane}$ (N)	263.80	220.14	309.92	482.43	272.01
$\sigma_f^{in-plane}$ (MPa)	12.50	10.43	14.69	22.86	12.89
$E_{eff}^{in-plane}$ (MPa)	266.74	334.80	240.04	519.37	392.21
$L_{\max}^{out-plane}$ (N)	46.77	74.37	62.25	99.38	53.22
$\sigma_f^{out-plane}$ (MPa)	13.86	22.03	18.44	29.44	15.77
$E_{eff}^{out-plane}$ (MPa)	829.34	1146.08	873.70	1817.75	1134.21
$L_{\max}^{Re}$ (mN)	244.51	274.17	301.69	327.71	337.91
R_f(%)	98.63	98.89	98.24	97.61	98.34
R_r(%)	99.53	99.52	99.63	99.56	99.64
t_{Re}	47 s	1 min 10 s	1 min 12 s	1 min 02 s	1 min 03 s

the highest recovery force ($L_{\max}^{Re}$) and ST-Re had the lowest, with values of 337.91 mN and 244.51 mN, respectively.

To study the shape memory behavior of 4D printed objects, the shape fixing ratio (R_f) of the samples after programming and the shape recovery ratio (R_r) during the recovery process were examined. R_f of different active sandwich structures is shown in table 1. Elastic deformation occured after

programming, and the R_f of sandwich structures was about 98%. The S-shaped curve in figure 7(c) shows the function of R_r with time. The samples recovered slowly at the beginning of heating. When the temperature reached the glass transition region, the deployment angle changed obviously. The release time of storage strain was different in figure 7(c). This can be attributed to the different heat conduction rates of different
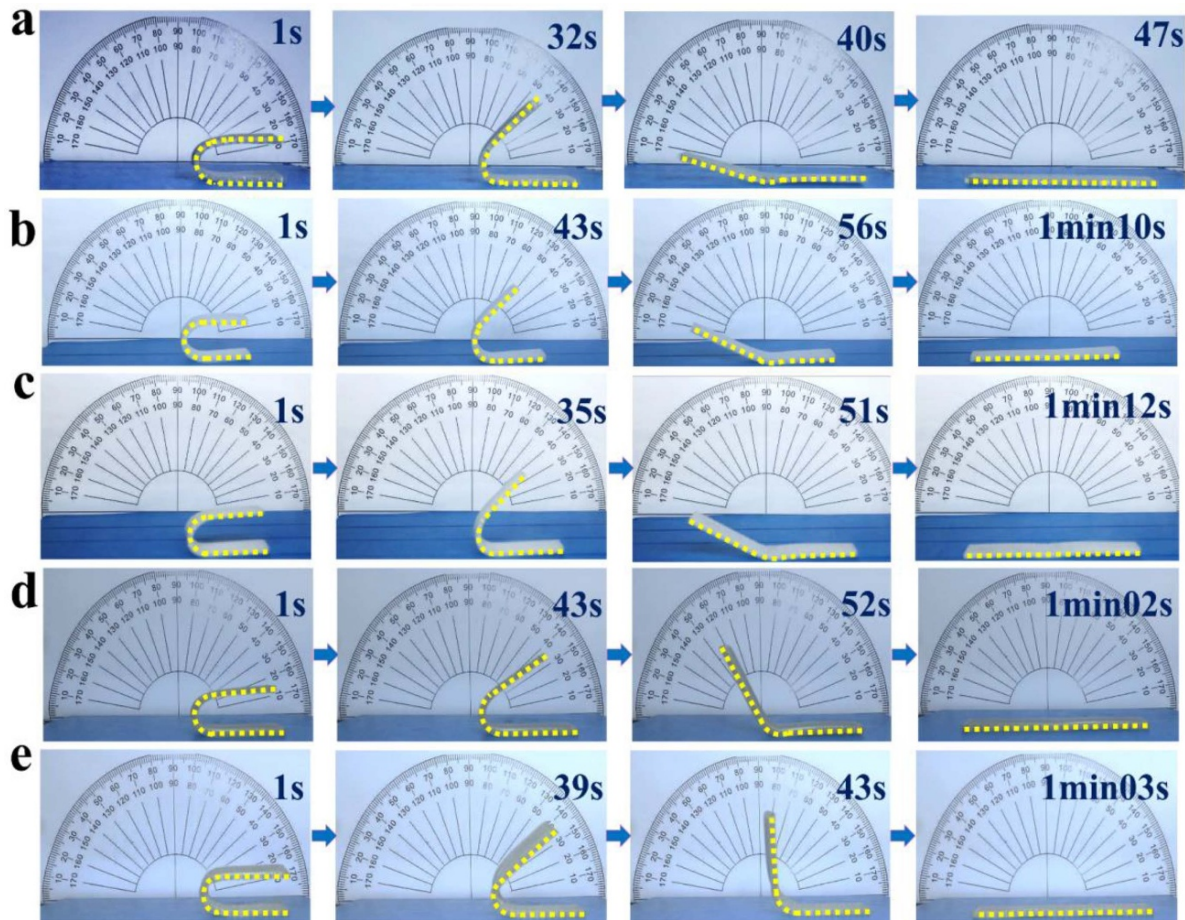
Figure 8. Shape memory recovery processes (a) ST-Re, (b) ST-6c, (c) ST-4c, (d) ST-St, and (e) ST-Do.

sandwich structures, resulting in different time required for the samples to reach the storage strain release temperature. The shape recovery ratio of the samples was over 99%. Figure 8 demonstrates the recovery process of active sandwich structures from U-shaped to flat state. The storage strain of the sample was activated after heating ~35 s and deployed within 60 s.

### 3.7. Shape recovery properties of origami structures

The thermomechanical cycle process of the origami-inspired structure was as follows: *i*. The sample was placed in hot water (90 °C) and folded according to the designed crease in figure 1; *ii*. The folded structure was cooled to room temperature. *iii*. The folded structure was placed in hot water (90 °C). The area change ratio of origami structures referred to the deployment/folding area ratio. It can intuitively reflect the folding performance of the structure and the ability to save space for packaging. The experimental results showed that different active sandwich also affect the area change ratio, the ratios of OS-Tw and OS-Sq were 261.41% and 375.45% respectively (figure 7(d)). Among the OS-AS, double arrowhead and re-entrant active sandwiches possessed the highest ratio (1134.61% and 1106.14% respectively), while star-shaped and hexa-chiral possessed the lowest ratio (1055.02% and

1058.46% respectively). This can be attributed to the different porosity of the structure, leading to the large area change ratio for OS-AS-Do and OS-AS-Re.

Figure 9 shows the deployment process of different origami structures after heating. Compared with heating by heat flow, the heat conduction of hot water was faster and the storage strain of origami structure was activated more rapidly. The storage strains of OT-Tw, OT-Sq, and OT-AS-Re were released as soon as they were immersed in water (~3 s). The origami structure exhibited a rapid response during the initial heating stage, and it took a longer time (~30 s) for the creases to recover to their original shape. This phenomenon was due to the large and complex deformation in the recovery process, and the thickness of the structure was also one of the influencing factors.

4. Conclusion

In this work, active sandwich structures with different honeycombs were fabricated by 4D printing. The thermally activated origami-inspired self-deployment sandwich structures with large area change ratio were developed. The in-plane tension and in-/out-plane three-point bending properties of active sandwichs were investigated. The results showed that
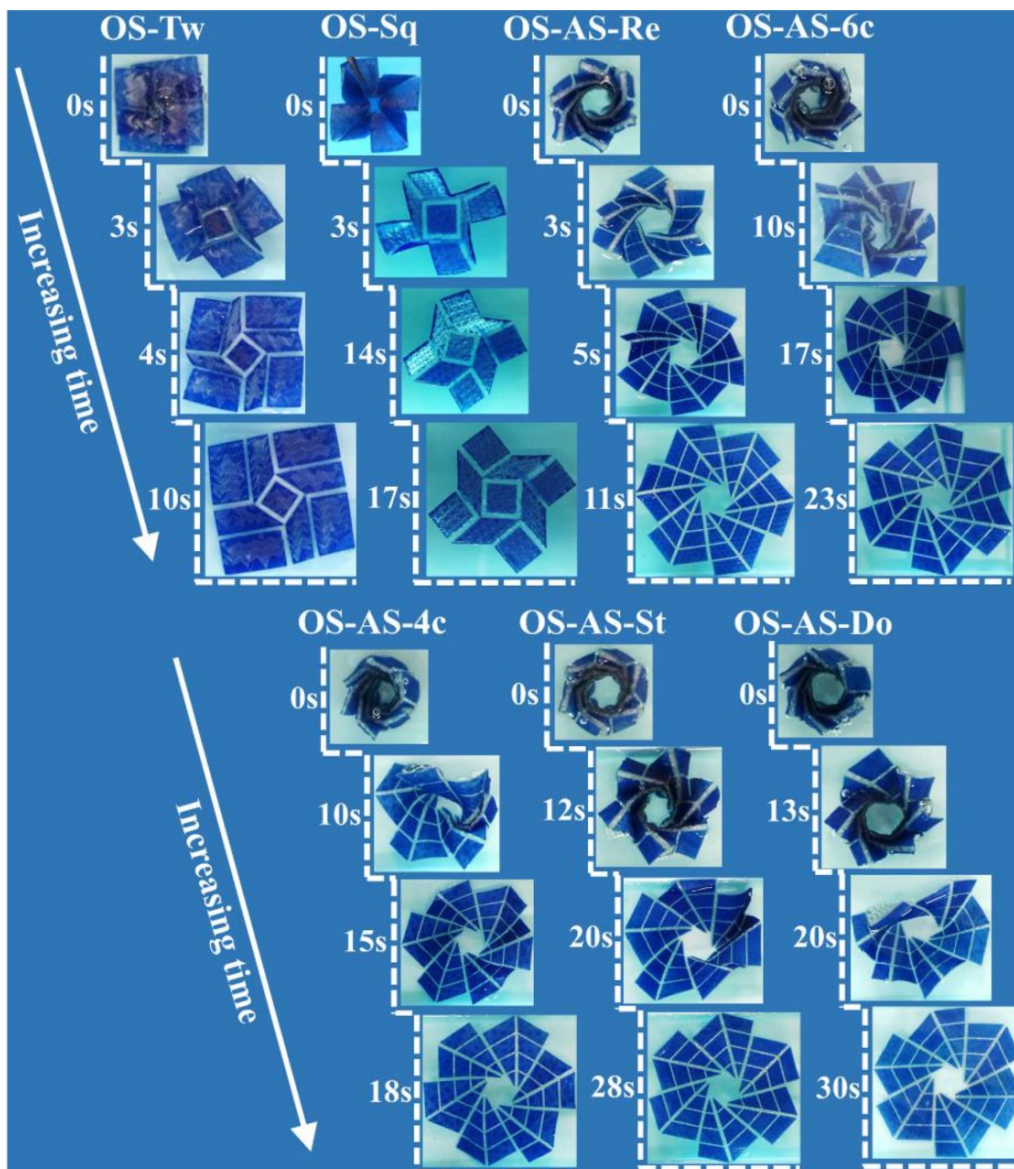
Figure 9. The shape memory recovery process of origami-inspired structures.

the strength and stiffness of ST-St were relatively high. The shape memory recovery tests exhibited that ST-Do possessed the highest recovery force of 337.91 mN. The designed sandwich structure had good shape memory performance, and the deployment time was ~1 min. Finally, the designed active sandwich origami-inspired structures demonstrated fast, large area change ratio and high precision self-deployment capabilities.

ORCID iDs

Xiaozhou Xin ⓘ https://orcid.org/0000-0001-5480-7051
Jinsong Leng ⓘ https://orcid.org/0000-0001-5098-9871

References

[1] Lendlein A and Gould O 2019 Reprogrammable recovery and actuation behaviour of shape-memory polymers *Nat. Rev. Mater.* **4** 116–33
[2] Zhao Q, Qi H and Xie T 2015 Recent progress in shape memory polymer: new behavior, enabling materials, and mechanistic understanding *Prog. Polym. Sci.* **49-50** 79–120
[3] Leng J, Lan X, Liu Y and Du S 2011 Shape-memory polymers and their composites: stimulus methods and applications *Prog. Mater. Sci.* **56** 1077–135

[4] Liu Y, Du H, Liu L and Leng J 2014 Shape memory polymers and their composites in aerospace applications: a review *Smart Mater. Struct.* **23** 023001

[5] Mu T, Liu L, Lan X, Liu Y and Leng J 2018 Shape memory polymers for composites *Compos. Sci. Technol.* **160** 169–98

[6] Xin X, Liu L, Liu Y and Leng J 2019 Mechanical models, structures, and applications of shape-memory polymers and their composites *Acta Mech. Solida Sin.* **32** 535–65

[7] Choong Y, Maleksaeedi S, Eng H, Wei J and Su P 2017 4D printing of high performance shape memory polymer using stereolithography *Mater. Des.* **126** 219–25

[8] Wagner M, Chen T and Shea K 2017 Large shape transforming 4D auxetic structures *3d Print Addit. Manuf.* **4** 133–41

[9] Akbari S, Sakhaei A, Kowsari K, Yang B, Serjouei A, Zhang Y and Qi G 2018 Enhanced multimaterial 4D printing with active hinges *Smart Mater. Struct.* **27** 065027

[10] Zhao W, Liu L, Zhang F, Leng J and Liu Y 2019 Shape memory polymers and their composites in biomedical applications *Mater. Sci. Eng.* C **97** 864–83

[11] Zhao W, Zhang F, Leng J and Liu Y 2019 Personalized 4D printing of bioinspired tracheal scaffold concept based on magnetic stimulated shape memory composites *Compos. Sci. Technol.* **184** 107866

[12] Kirillova A and Ionov L 2019 Shape-changing polymers for biomedical applications *J. Mater. Chem.* B **7** 1597–624

[13] Wang Y, Villada A, Zhai Y, Zou Z, Chen Y, Yin X and Xiao J 2019 Tunable surface wrinkling on shape memory polymers with application in smart micromirror *Appl. Phys. Lett.* **114** 193701

[14] Wang X *et al* 2019 Freestanding 3D mesostructures, functional devices, and shape-programmable systems based on mechanically induced assembly with shape memory polymers *Adv. Mater.* **31** 1805615

[15] Boyraz P, Runge G and Raatz A 2018 An overview of novel actuators for soft robotics *Actuators* **7** 48

[16] Lin C, Lv J, Li Y, Zhang F, Li J, Liu Y, Liu L and Leng J 2019 4D-printed biodegradable and remotely controllable shape memory occlusion devices *Adv. Funct. Mater.* 1906569

[17] Ge Q, Dunn C, Qi H and Dunn M 2014 Active origami by 4D printing *Smart Mater. Struct.* **23** 094007

[18] Zirbel S, Magleby S, Howell L, Lang R, Thomson M, Sigel D, Walkemeyer P and Trease B 2014 Accommodating thickness in origami-based deployable arrays *Proc. of the Asme Int. Design Engineering Technical Conf.s and Computers and Information in Engineering Conf. (DECT 2013)* V06BT07A027

[19] Schenk M, Viquerat A, Seffen K and Guest S 2014 Review of inflatable booms for deployable space structures: packing and rigidization *J. Spacecr. Rockets* **51** 762–78

[20] Filipov E, Tachi T and Paulino G 2015 Origami tubes assembled into stiff, yet reconfigurable structures and metamaterials *Proc. Natl Acad. Sci. USA* **112** 12321–6

[21] Ning X, Wang X, Zhang Y, Yu X, Choi D, Zheng N, Kim D, Huang Y, Zhang Y and Rogers J 2018 Assembly of advanced materials into 3d functional structures by methods inspired by origami and kirigami: a review *Adv. Mater. Interfaces* **5** 1800284

[22] Yan Z *et al* 2017 Controlled mechanical buckling for origami-inspired construction of 3D microstructures in advanced materials (vol 26, 2629, 2016) *Adv. Funct. Mater.* **27**

[23] Callens S and Zadpoor A 2018 From flat sheets to curved geometries: origami and kirigami approaches *Mater. Today* **21** 241–64

[24] Thesiya D, Srinivas A and Shukla P 2015 A novel lateral deployment mechanism for segmented mirror/solar panel of space telescope *J. Astron. Instrum.* **4** 1550006

[25] Gruber P, Hauplik S, Imhof B, Ozdemir K, Waclavicek R and Perino M 2007 Deployable structures for a human lunar base *Acta Astronaut.* **61** 484–95

[26] Kim T and Lee Y 2018 Shape transformable bifurcated stents *Sci. Rep.* **8** 13911

[27] Ge Q, Qi H and Dunn M 2013 Active materials by four-dimension printing *Appl. Phys. Lett.* **103** 131901

[28] Neville R, Pirrera A and Scarpa F 2014 Open shape morphing honeycombs through kirigami *Proc. Asme. Conf. Smart Materials, Adaptive Structures and Intelligent Systems (SMASIS 2014)* V001T01A010

[29] Gladman A, Matsumoto E, Nuzzo R, Mahadevan L and Lewis J 2016 Biomimetic 4D printing *Nat. Mater.* **15** 413-+

[30] Gonzalez-Henriquez C, Sarabia-Vallejos M and Rodriguez-Hernandez J 2019 Polymers for additive manufacturing and 4D-printing: materials, methodologies, and biomedical applications *Prog. Polym. Sci.* **94** 57–116

[31] Momeni F, Hassani N, Liu X and Ni J 2017 A review of 4D printing *Mater. Des.* **122** 42–79

[32] Gao B, Yang Q, Zhao X, Jin G, Ma Y and Xu F 2016 4D Bioprinting for biomedical applications *Trends Biotechnol.* **34** 746–56

[33] Felton S, Tolley M, Demaine E, Rus D and Wood R 2014 A method for building self-folding machines *Science* **345** 644–6

[34] Mao Y, Yu K, Isakov M, Wu J, Dunn M and Qi H 2015 Sequential self-folding structures by 3D printed digital shape memory polymers *Sci. Rep.* **5** 13616

[35] Yu K, Ritchie A, Mao Y, Dunn M and Qi H 2015 Controlled sequential shape changing components by 3D printing of shape memory polymer multimaterials *Proc. Iutam* 193–203

[36] Wu J, Yuan C, Ding Z, Isakov M, Mao Y, Wang T, Dunn M and Qi H 2016 Multi-shape active composites by 3D printing of digital shape memory polymers *Sci. Rep.* **6** 24224

[37] Yuan C, Wang T, Dunn M and Qi H 2017 3D printed active origami with complicated folding patterns *Int. J. Precis. Eng. Manuf. Green* **4** 281–9

[38] Liu Y *et al* 2018 Shape memory behavior and recovery force of 4D printed laminated Miura-origami structures subjected to compressive loading *Composites* B **153** 233–42

[39] Wang L, Song W and Fang D 2019 Twistable origami and kirigami: from structure-guided smartness to mechanical energy storage *Acs Appl. Mater. Inter.* **11** 3450–8

[40] Kolken H and Zadpoor A 2017 Auxetic mechanical metamaterials *Rsc. Adv.* **7** 5111–29

[41] Mir M, Ali M, Sami J and Ansari U 2014 Review of mechanics and applications of auxetic structures *Adv. Mater. Sci. Eng.* **2014** 753496

[42] Carneiro V, Meireles J and Puga H 2013 Auxetic materials - A review *Mater. Sci. Poland.* **31** 561–71

[43] Al-Mulla T and Buehler M 2015 Folding creases through bending *Nat. Mater.* **14** 366–8

[44] Morgan J, Magleby S and Howell L 2016 An approach to designing origami-adapted aerospace mechanisms *J. Mech. Des.* **138** 052301

[45] Zhang F, Wang L, Zheng Z, Liu Y and Leng J 2019 Magnetic programming of 4D printed shape memory composite structures *Composites* A **125** 105571

[46] Liu Y, Zhang W, Zhang F, Leng J, Pei S, Wang L, Jia X, Cotton C, Sun B and Chou T 2019 Microstructural design for enhanced shape memory behavior of 4D printed composites based on carbon nanotube/polylactic acid filament *Compos. Sci. Technol.* **181** 107692